



Frequency-domain energy transport state-resolved Raman for measuring the thermal conductivity of suspended nm-thick MoSe₂



Hamidreza Zobeiri^{a,1}, Ridong Wang^{a,1}, Tianyu Wang^a, Huan Lin^b, Cheng Deng^{c,*}, Xinwei Wang^{a,*}

^a Department of Mechanical Engineering, Iowa State University, Ames, IA 50011, United States

^b School of Environmental and Municipal Engineering, Qingdao University of Technology, Qingdao, Shandong 266033, PR China

^c College of Mechatronics Engineering, Guangdong Polytechnic Normal University, Guangzhou 510635, PR China

ARTICLE INFO

Article history:

Received 6 October 2018

Received in revised form 1 December 2018

Accepted 2 January 2019

Keywords:

In-plane thermal conductivity

Frequency modulation

Energy transport state design

nm-thick MoSe₂

ABSTRACT

Temperature-dependent Raman properties calibration and laser absorption evaluation are two significant sources of error in measurement of nm-thick materials thermal conductivity based on steady state Raman spectroscopy. A new Raman probing technique, frequency-domain energy transport state-resolved Raman (FET-Raman), is developed to resolve these issues and improve the measurement precision significantly. The FET-Raman uses a steady-state laser and an amplitude-modulated square wave laser for heating the material and simultaneous exciting Raman signals. Under these two energy transport states, Raman-shift power coefficients for both states are determined, and their ratio is used to determine the in-plane thermal conductivity of nm-thick material. Four MoSe₂ samples with different thicknesses (5–80 nm) suspended on a circular hole are used to explore the capability of this new technique. The in-plane thermal conductivity of these samples increases from 6.2 ± 0.9 to 25.7 ± 7.7 W·m⁻¹·K⁻¹ with increased thickness. This is attributed to the increment of surface phonon scattering effect for thinner samples. The FET-Raman technique provides a novel way to measuring thermal conductivity of nm-thick materials with high accuracy and great ease of implementation.

© 2019 Elsevier Ltd. All rights reserved.

1. Introduction

Thermal characterization of 2D atomic-layer materials [1] such as graphene [2–6], black phosphorus [7–10], molybdenum disulfide [11–13], and molybdenum diselenide [14] has been the focus of several recent research. The optothermal method based on Raman spectroscopy has proved nondestructive for thermal properties measurement with a high spatial resolution, easy sample preparation, and simple experiment setup [5,6,15–22]. To date, several research groups have used this method to measure the thermal conductivity of suspended samples. Lee et al. [23] reported the thermal conductivity of suspended single-layer graphene as a function of temperature using this method. Peimyo et al. [24] determined the thermal conductivity of suspended mono- and bilayer WS₂ by Raman spectroscopy. Luo et al. [25] measured the anisotropic in-plane thermal conductivity of suspended black

phosphorus samples using the micro Raman technique. However, while using this method, a relationship between temperature and Raman spectrum needs to be established using calibration to measure a temperature coefficient. Also, laser absorption needs to be determined with high accuracy. The measurement of temperature coefficient and laser absorption are significant sources of error.

To fix the abovementioned drawbacks, a time-domain differential Raman (TD-Raman) was developed in our lab by modulating the excitation laser and probing transient Raman scattering during the pulsed laser heating [26]. Instead of studying the instant specific temperature of sample, it only needs the normalized variation of the temperature rise to be studied using TD-Raman. Li et al. [27] determined the thermal diffusivity and thermal conductivity of carbon nanotube fiber by TD-Raman. However, when the heating time is too short, it becomes very challenging to study the thermal transport phenomena. Also, the materials with less crystalline structure, it makes it difficult to do TD-Raman measurement [27].

To overcome the drawbacks of TD-Raman on short time thermal probing, Wang et al. [28] developed a frequency-resolved Raman (FR-Raman) method. To characterize the thermal diffusivity of a microscale silicon cantilever, the steady state laser is modulated in square-wave form in a wide range of frequencies. Using the

* Corresponding authors at: 271 Applied Science Complex II, Department of Mechanical Engineering, Iowa State University, Ames, IA 50011, United States (X. Wang).

E-mail addresses: 275195971@qq.com (C. Deng), xwang3@iastate.edu (X. Wang).

¹ H. Zobeiri and R. Wang contributed equally to this work.

fitted values of wavenumber, Raman intensity, and emission against frequency, the thermal diffusivity of the sample is determined. In addition, Wang et al. [29] put one more step forward and determined the anisotropic thermal conductivity of suspended black phosphorus sample using the FR-Raman method. In this work, an “as transferred” and a “laser modified” samples are used to do the experiment. Using the ratio of the power differential of the wavenumber of these two samples, the ratio of the armchair thermal conductivity (κ_{AC}) and zigzag thermal conductivity (κ_{ZZ}) is obtained. After that, the absolute values of κ_{AC} and κ_{ZZ} are extracted from the normalized average temperature, which is determined from the measurement of wavenumber against different frequencies.

Yuan et al. [30] measured the hot carrier diffusion coefficient (D) and the interface thermal resistance (R) using the energy transport state-resolved Raman (ET-Raman) technique that they developed in our lab. With this great method, D and R of few-layered MoS₂ are measured without the need of laser absorption evaluation and Raman property temperature coefficient calibration. In this method, sample is irradiated with a picosecond laser as the near zero-transport case and a CW laser as the steady state case. D and R are determined by comparing the Raman wavenumber shift measured from different energy transport states. Yuan et al. [31] took one more step forward and simultaneously determined the in-plane κ , R , and D of MoS₂ thin films that are supported on glass substrate. In this work, five-state ET-Raman with energy transport in both space and time domains is developed to take into account the effects of interface thermal resistance and electron diffusivity on measurement of in-plane κ . Wang et al. [32] employed this ET-Raman method to measure the in-plane thermal conductivity of suspended 2D atomic-layer materials. However, since a strong heat accumulation happens during the irradiation of the suspended samples with ps laser, a nanosecond pulsed laser is used. By studying the power differential of Raman shift under these two energy transport states, the thermal conductivity of several 2D MoS₂ and MoSe₂ samples is measured.

In this work, we developed a Frequency Domain Energy Transport state-resolved Raman (FET-Raman) technique based on the FR-Raman and ET-Raman techniques for measuring the thermal conductivity of nm-thick materials. In this technique, unlike the ET-Raman that we need two different lasers to perform the experiment, we just do that with a CW laser and a modulator to modulate the steady state laser in a square-wave form in a specific frequency. Therefore, the experiment setup is significantly simplified. Using this novel method, the in-plane thermal conductivity of suspended MoSe₂ is measured. The effect of sample thickness on in-plane thermal conductivity of this material in the range of 5–80 nm is reported. Also, the effects of laser absorption coefficient and modulation frequency on the measured in-plane thermal conductivity are studied in detail to prove the robustness of the technique.

2. Physical principles and experimental details

In the FET-Raman technique, we probe the thermal response of the material by irradiating the samples using a steady-state (CW) laser with 532 nm wavelength. Fig. 1 shows the physical principle of this technique. In the first step as shown in Fig. 1(a) and (b), the steady state case, the center of suspended sample is irradiated with the CW laser. During the irradiation, the sample absorbs the laser energy and its temperature increases. The amount of temperature rise of the sample is related to its thermal conductivity. By collecting the excited Raman signals during the laser heating, we can obtain the temperature profile of the suspended sample. Note here we do not need to measure the real temperature rise of the sample.

Using different laser powers (P), we can get the Raman shift power coefficient (RSC) in the steady state case which is dependent on laser absorption coefficient (α), temperature coefficient of Raman shift ($\partial\omega/\partial T$), and the in-plane thermal conductivity (κ): $\psi_{CW} = \partial\omega/\partial P \propto \alpha(\partial\omega/\partial T)/\kappa$.

In the second step as shown in Fig. 1(c) and (d), we utilize a square-wave modulated laser with a specific frequency to induce the heating effect and excite Raman scattering. In each period of this modulated laser, there is a laser-on time (τ_h) and a laser-off time (τ_c). τ_h is equal to τ_c . Note here τ_h and τ_c do not need to be equal. Making them equal will ease the Raman measurement significantly and significantly simplify the data processing. If τ_h and τ_c are not equal, the TD-Raman method can be used, which is detailed in our previous work [26]. Based on the frequency of the modulated laser, two possible states can exist: (1) quasi-steady state, and (2) steady-state (Fig. 1(e) and (f)) [28]. When the frequency is very high, the temperature variation during the τ_h and τ_c is very small, so the temperature can be regarded as a constant. This state is the quasi-state and the average temperature rise during τ_h is θ_{qs} . When the frequency is very low, during τ_h the temperature reaches the steady-state and during the τ_c returns to the initial point. This case is called steady-state and its average temperature rise during τ_h is θ_s . From a high frequency to a low frequency, thermal response changes gradually from “quasi-steady state” to “steady-state” case and the average temperature rise during τ_h varies from θ_{qs} to θ_s . It is proved that $\theta_{qs} = \theta_s/2$ [29]. As shown in Fig. 1(f), during each laser-on time, there is a transient state (t_r) for temperature rise and if the frequency is low enough, it can reach the steady state (t_s). After several heating and cooling states, the sample reaches a steady periodic thermal state [29]. Under frequency-modulated laser irradiation, the effective thermal diffusion length in the thickness direction ($L_{d\perp}$) could be estimated as: $L_{d\perp} = \sqrt{\pi\alpha_{\perp}/f}$, where α_{\perp} (m²/s) and f (Hz) are thermal diffusivity in cross-plane direction and modulation frequency, respectively. The diffusion length of MoSe₂ is about 7 μ m for $f = 100$ kHz. Since the thickness of the sample, which is less than 100 nm, is much less than $L_{d\perp}$, the thermal transport in the cross-plane direction can be neglected. Therefore, it is physically reasonable to take a constant temperature in the thickness direction. Such constant temperature also has been proved by our detailed modeling as discussed in Section 3.1. By choosing an appropriate frequency and collecting the Raman signals during the heating time using different laser powers, we can obtain the RSC value in frequency-resolved Raman state: $\psi_{FR} = \partial\omega/\partial P \propto \alpha(\partial\omega/\partial T)/(\rho c_p) f (\kappa/\rho c_p)$. In this work, the modulation frequency takes 100 kHz. This frequency is around the middle of quasi-steady state to steady state range based on our preliminary study. Using the ψ_{CW} and ψ_{FR} , a normalized RSC value could be calculated as: $\Theta = \psi_{FR}/\psi_{CW}$. By doing so, the effect of laser absorption coefficient and Raman temperature coefficient is eliminated. In addition, since the volumetric heat capacity (ρc_p) of the suspended sample has negligible size effect and can be readily obtained from Refs. [33,34], the value of Θ is only dependent on the in-plane thermal conductivity as:

$$\frac{\psi_{FR}}{\psi_{CW}} \propto \frac{\alpha(\partial\omega/\partial T)/(\rho c_p) f (\kappa/\rho c_p)}{\alpha(\partial\omega/\partial T)/\kappa} = \frac{\kappa}{(\rho c_p) f (\kappa/\rho c_p)} \quad (1)$$

To find the unknown in-plane thermal conductivity of the sample, a 3D heat conduction model is used to simulate the temperature rise under the two energy transport states. Using this simulation, we can find the theoretical relationship between the ratio of temperature rise in the two cases and in-plane thermal conductivity. Finally, the in-plane thermal conductivity of different thickness samples could be determined based on the measured.

For the steady-state heating, the governing equation is [23,35]:

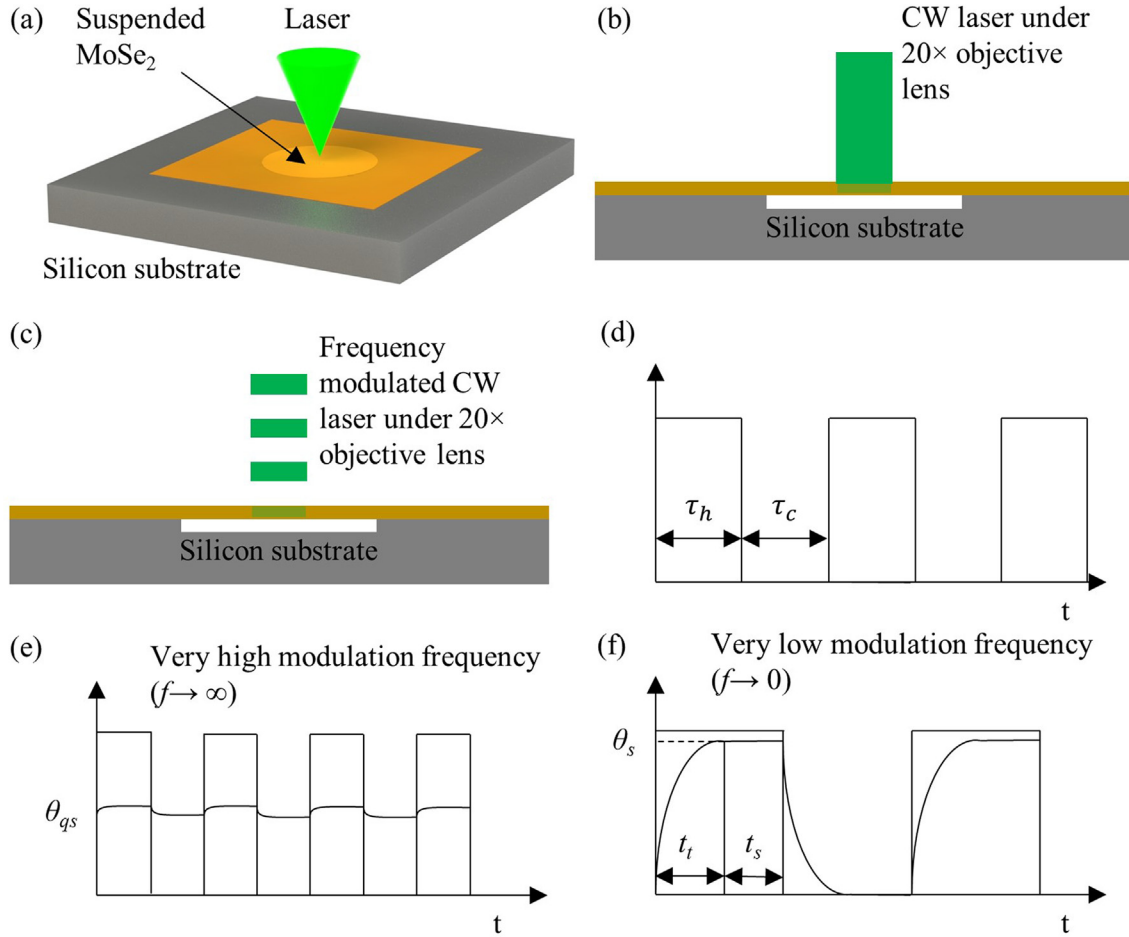


Fig. 1. Illustration of physical concept of the experiment. (a) Examined MoSe₂ nanosheets are placed onto a silicon substrate with a circular hole and irradiated with a 532 nm continuous-wave (CW) laser. (b) Schematic of MoSe₂ sample suspended on c-Si substrate under CW laser and (c) under frequency-modulated laser. (d) Concept of FET-Raman technique. (e) The quasi-steady state under very high modulation frequency. (f) The steady state under very low modulation frequency.

$$\kappa \nabla^2 T_{CW} + \dot{q} = 0 \quad (2)$$

where T_{CW} is temperature rise in steady-state case, κ ($\text{W}\cdot\text{m}^{-1}\cdot\text{K}^{-1}$) is in-plane thermal conductivity, and \dot{q} is the volumetric Gaussian beam heating as below [32]:

$$\dot{q}(r, z) = I_0/\tau_L \exp(-r^2/r_0^2) \exp(-z/\tau_L) \quad (3)$$

where $I_0 = P/\pi r_0^2$ is the laser power per unit area in center of laser spot, r_0 (μm) is the radius of the laser spot, τ_L is laser absorption depth. And $\tau_L = \lambda/(4\pi k_L)$ [36] where λ is the laser wavelength (532 nm), and k_L is the extinction coefficient of the sample. So, τ_L (MoSe₂) = 20.6 nm [37,38]. Note although we need this extinction coefficient for data processing, any uncertainty in k_L will have negligible effect in our final measured κ for two reasons. First, the overall laser absorption is canceled in Θ calculation. Second, since the sample is very thin (few to tens of nm), the temperature is uniform in the thickness direction, and has negligible effect from the volumetric laser absorption.

The temperature distribution induced by absorption of laser irradiation in the frequency-resolved Raman state is determined by the following equation [39]:

$$\kappa \nabla^2 T_{FR} + \dot{q} = \rho c_p (\partial T_{FR} / \partial t) \quad (4)$$

where T_{FR} is the temperature rise in the transient state and \dot{q} could be calculated as Eq. (3). Here we take ρc_p constant because the temperature rise by the laser heating is moderate (discussed in Section 3.3). As a result, using the last two governing equations, the

ratio of temperature rises as a function of in-plane thermal conductivity of the sample is obtained. In the experiment, this ratio is equal to normalized RSC value.

Fig. 2 shows the Raman system setup of the experiment. The atomic structure of MoSe₂ is shown in Fig. 2(b). Two vibrational modes exist: A_{1g} out-of-plane modes and E_{2g}^1 in-plane mode [40,41]. In the A_{1g} mode, two Se atoms oscillate with respect to the Mo atom which is in the center [40]. E_{2g}^1 mode exists at higher wavenumbers than A_{1g} mode and its intensity is weaker than A_{1g} . Tongay et al. [41] measured the ratio of the intensity of these peaks ($I_{A_{1g}}/I_{E_{2g}^1}$) using a 488 nm laser and observed that this ratio increases from 4.9 for few-layer (~ 10 layers) to 23.1 for single-layer MoSe₂. As shown in Fig. 2(c), we could not observe the E_{2g}^1 peak under 532-nm laser excitation. Therefore, here we use the A_{1g} peak to determine the RSC value based on the acquired Raman spectra.

As shown in Fig. 2(a), the FET-Raman system consists of a 532-nm CW laser (Excelsior-532-150-CDRH Spectra-Physics) as an energy source, a Raman spectrometer (Voyage, B&W Tek, Inc.), and a microscope (Olympus BX53). This laser source is modulated in a square-wave form using an electro-optics modulator (EOM). Using a function generator, the laser could be modulated in various frequencies as high as 20 MHz. In addition, a motorized neutral-density (ND) filter (CONEX-NSR, Newport Corporation) is utilized to adjust the laser power. The ND filter and Raman spectrometer are controlled by a LabVIEW-based software. As a result, the

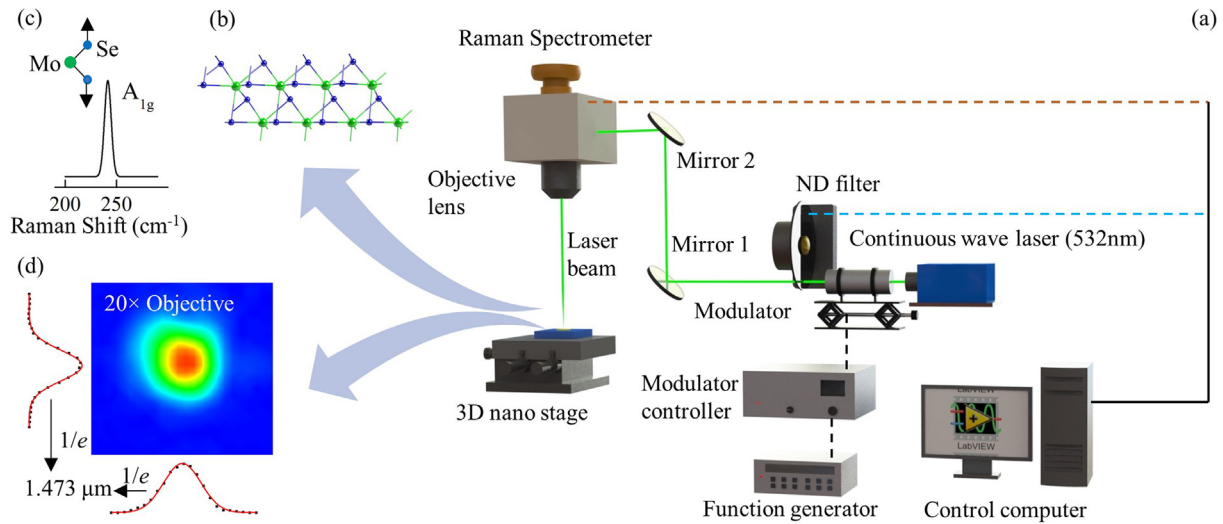


Fig. 2. Schematic of FET-Raman experimental setup. (a) A MoSe₂ sample is illuminated by the CW laser and its frequency-modulated case. The modulation frequency could be controlled by a function generator. A ND filter is used to adjust the laser power. A LabVIEW-based program is used to control the ND filter and Raman spectrometer. (b) The atomic structure of MoSe₂. The big green balls are Mo atoms, and small blue atoms stand for Se atoms. (c) Raman spectrum of MoSe₂ excited by 532 nm laser. A_{1g} (~240 cm⁻¹) mode is observed for all four samples and is employed to explore the temperature rise. (d) The spatial energy distribution of the laser beam and spot size are measured with a CCD camera. The black points are laser beam intensity data taken from the CCD camera images. The red curve shows the data fitting using the Gaussians function. The laser beam radius (at e^{-1}) on the sample is determined as 1.473 μm under 20 \times objective lens.

accuracy of the experiment is improved significantly, and its time is reduced considerably. The laser beam is focused by a 20 \times objective lens (NA = 0.4). The hot carrier diffusion length for MoSe₂ is estimated based on equation $L_c = \sqrt{\tau D}$, where τ is the lifetime of the hot carriers and D is hot carrier diffusivity. Since τ is in order of 100 ps [42,43] and $D = 11 \times 10^{-6} \text{ m}^2/\text{s}$ [44], the hot carrier diffusion length is in the order of 10 nm. Since this diffusion length is much shorter than the laser spot size under 20 \times objective lens, the effect of hot carrier transfer becomes negligible. The optical images of the laser spots are captured with a CCD (charge-coupled-device) camera (Olympus DP-26, Olympus Optical Co., Ltd.). Then these images are analyzed based on a Gaussian fitting method to calculate the radius of the laser spots. Fig. 2(d) shows the laser spot size measurement of the 36 nm sample. The spot radius is defined at the location where the laser intensity decays to e^{-1} of the peak value.

Four few-layered MoSe₂ samples are prepared by mechanical exfoliation. This technique is one of the simplest and most reliable ones to prepare highly crystalline and atomically thin nanosheets of layered materials [12,45]. These samples are transferred to a clean silicon substrate with a circular hole, $D = 10 \mu\text{m}$ and depth of 3 μm , on its center. Details of sample preparation could be found in the previous works of our group [29,30].

3. Results and discussion

3.1. Thermal conductivity determination

Fig. 3(a)–(d) show AFM images of four suspended MoSe₂ samples. To avoid damaging the samples on suspended areas, the thickness of supported area near the suspended area is measured. The height profile below each image is corresponding to the red dashed line in that AFM image. The samples have a thickness of 5, 36, 55, and 80 nm, respectively. In addition, the roughness profile of each surface is included for each sample surface. Δl_{max} is the biggest thickness variation along a line on the sample surface. For the sample with 36 nm thickness, Δl_{max} is larger than that of two thicker samples. It could be due to the wrinkles on this sample.

The 36 nm-thick sample is used to illustrate the results. Table 1 indicates the laser power range and laser spot size for this sample as well as other three samples. The obtained values of the radius (at e^{-1} of the center intensity) of the laser spots on the four samples are also listed in Table 1. There are some differences among the laser spot on different samples. These differences are mainly induced by the slight variation in focusing level for each sample. However, since these actual values are used to do numerical calculation for each sample, this variation in laser spot size does not affect the results.

Fig. 4(a) and (b) show the 3D contour map of the MoSe₂ Raman peak under different laser powers. The Raman intensity increases linearly with the increased laser power. Errors in the Gaussian fitting of the Raman spectra and the effect of laser heating are two possible reasons that can cause deviation from linearity. As the laser irradiates the sample, the local temperature of the sample increases, and as a result, the detected Raman intensity will decrease. Additionally, Fig. 4(c) and (d) show the contour maps of Raman peak and indicates the redshift of laser peak with increased laser power. Five representative room temperature Raman spectra of this sample for both CW and FR cases are shown in Fig. 5(a) and (b), respectively. It also indicates the redshift of Raman peak with the increased laser power.

Fig. 5(c) and (d) show the linear dependency of Raman shift and laser power in low-power range for both CW and FR cases. The linear fitting results RSC of A_{1g} mode under CW laser is $-1.155 \pm 0.017 \text{ cm}^{-1}/\text{mW}$, and for the FR case is $-0.983 \pm 0.022 \text{ cm}^{-1}/\text{mW}$. RSC values for all the four MoSe₂ samples are included in Table 2. As shown in Table 2, the RSC value of both CW and FR cases decreases with increased sample thickness. This trend indicates the increase of κ with increased sample thickness. This is because when ψ is lower, it means the sample has a lower temperature rise under the same laser heating, meaning the sample has a better capability (higher κ) to dissipate the absorbed laser energy.

The normalized RSC values (Θ) of all four samples are indicated in Table 2. As shown in Table 2, Θ increases with increasing of thickness. For each sample, Θ indicates how fast the suspended sample reaches the steady state. In fact, higher Θ values mean a shorter transient time. Therefore, it is reasonable for the thicker

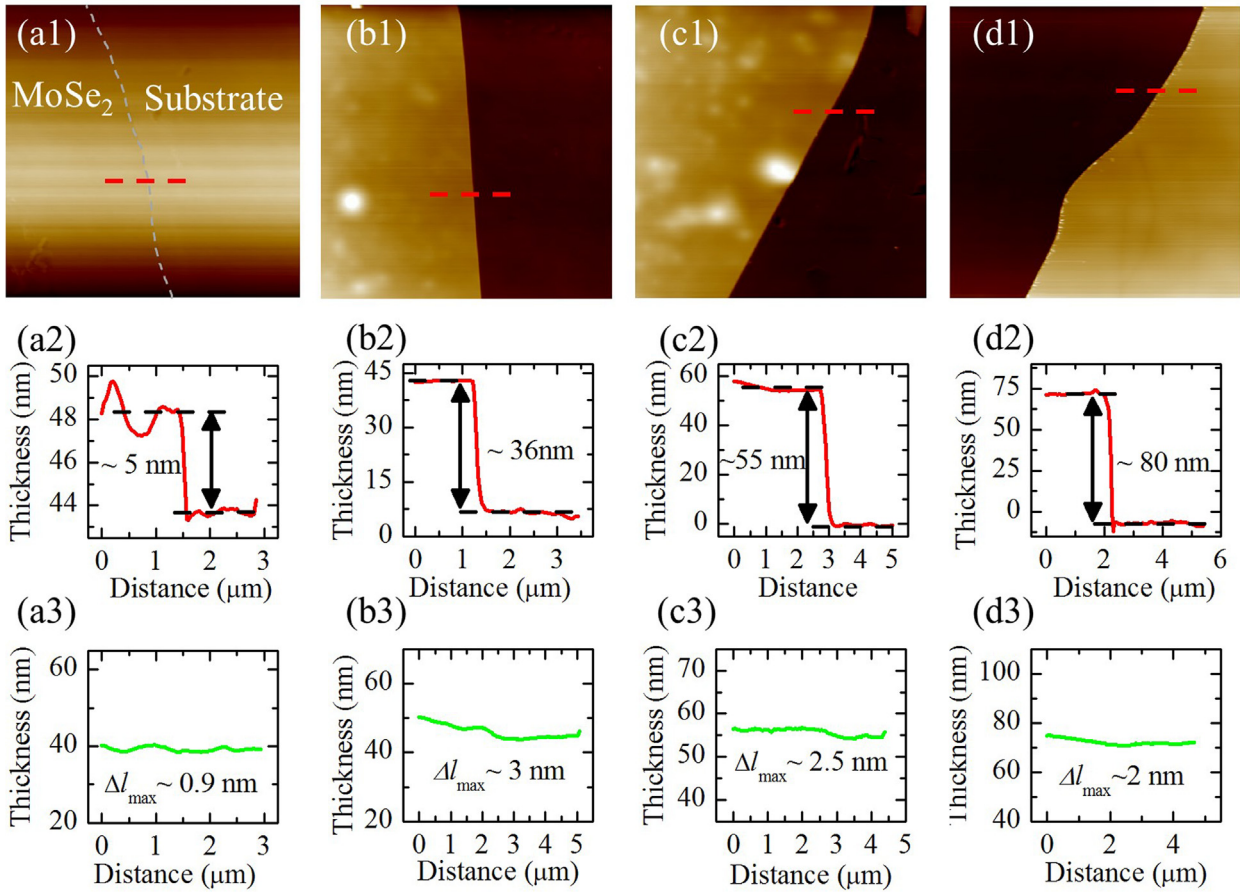


Fig. 3. AFM measurement results of four MoSe₂ samples. (a1–d1) AFM images of all samples. Gray dashed line in (a1) indicates the boundary between MoSe₂ film and substrate. (a2–d2) Thickness profiles corresponding to the red dashed line in figures (a1–d1). (a3–d3) Thickness profiles to indicate the roughness of measured area.

Table 1
Laser power range for four samples and laser spot radius for each one.

Sample thickness (nm)	Laser spot radius (μm)	Laser power range under 20× objective lens (mW)
5	1.634	0.084–0.405
36	1.473	0.392–1.897
55	1.549	0.426–2.063
80	1.993	0.458–2.219

samples that have a higher κ to reach the steady state temperature faster than the thinner ones.

To obtain the theoretical values of temperature rise for both steady state and transient state, 3D modelling based on the finite volume method is conducted. During the simulation, the measured laser spot sizes are used, as shown in Table 1. Also, the volumetric absorption of the laser beam is considered rigorously. Since the temperature ratio of two cases is not relevant to \dot{q} and cross-plane thermal conductivity, this ratio can be calculated under the arbitrary setting values of \dot{q} and cross-plane thermal conductivity. Raman intensity weighted average temperature over space and time domain for both CW and FR cases are considered. For the CW case, over the space domain, the average temperature is calculated using the following equation [32]:

$$\bar{T}_{CW} = \int_0^{V_0} I e^{-z/\tau_L} T dv / \int_0^{V_0} I e^{-z/\tau_L} dv, \quad (5)$$

where T is the temperature of each point of the sample, and I is the laser intensity that is given by Eq. (3). The term e^{-z/τ_L} in Eq. (5) is for

the Raman signal attenuation when it leaves the original scattering location. For the FR case, the Raman intensity weighted average temperature is calculated over time domain as well as the space domain as [32]:

$$\bar{T}_{FR} = \int_0^t \int_0^{V_0} I e^{-z/\tau_L} T dv dt / \int_0^t \int_0^{V_0} I e^{-z/\tau_L} dv dt. \quad (6)$$

Fig. 6 shows the temperature rise of the 36 nm sample under laser heating at different time using its determined thermal conductivity of $10.8 \text{ W}\cdot\text{m}^{-1}\cdot\text{K}^{-1}$ and an arbitrary heating power of $\dot{q} = 0.01 \text{ mW}$. For this case, heating time is equal to $5 \mu\text{s}$ because the modulation frequency is 100 kHz. Here, the cross-plane thermal conductivity takes $3 \text{ W}\cdot\text{m}^{-1}\cdot\text{K}^{-1}$ [33,46]. Fig. 6(a1)–(h1) show the top view and Fig. 6(a2)–(h2) show the cross-sectional view of the sample. The sample reaches the steady state within the half of the heating time. It is also noted although the laser heating at different depth is different due to the volumetric absorption, the heat transfer in the thickness direction is very fast with respect to the very small thickness. Therefore, the temperature distribution in the thickness direction is very uniform. In our data processing using Eq. (6), the temperature evolution and distribution as demonstrated in Fig. 6 all are considered.

3.2. Effect of film thickness on thermal conductivity

Using the ratio of \bar{T}_{CW} and \bar{T}_{FR} , the theoretical curve of Θ versus κ is determined. As shown in Fig. 7(a), using this theoretical curve and experimental Θ , the value of in-plane κ could be interpolated. Table 3 shows the measured thermal conductivity of four MoSe₂

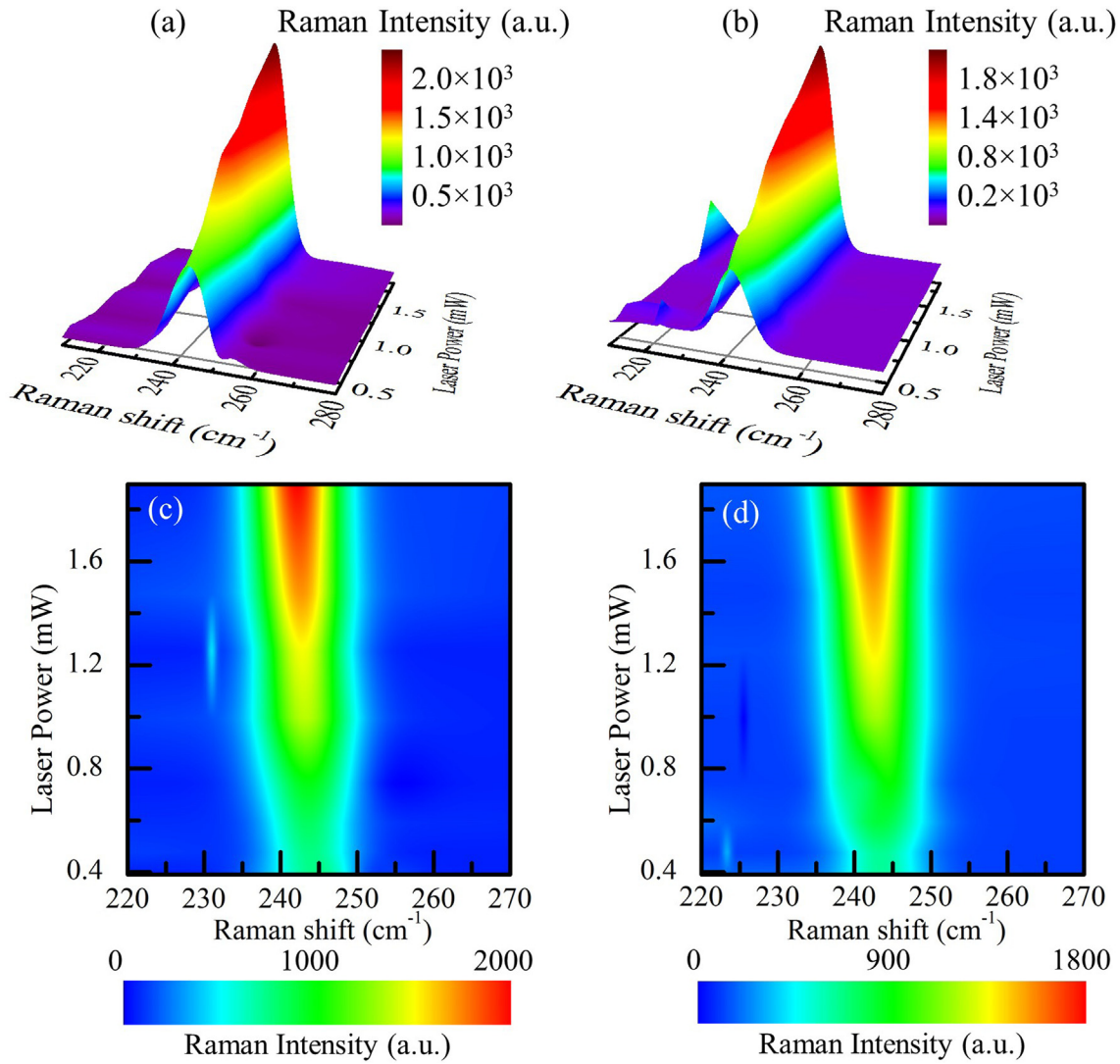


Fig. 4. Contour maps of MoSe₂ Raman peaks. The 36 nm-thick sample is used to illustrate the results. (a) and (b) The variation of Raman intensity against laser power for both CW and FR cases, respectively, using 3D contour maps. (c) and (d) Indicate 2D contour maps of Raman shift against laser power for both CW and FR cases, respectively.

samples against their thickness. In order to elucidate how the κ value changes with MoSe₂ thickness, we have plotted the measured κ values of MoSe₂ in this work and other works as a function of MoSe₂ thickness, from monolayer to bulk, as shown in Fig. 7(b) [17,33,46–49]. For monolayer and few-layered samples, both theoretical and experimental results show a decreasing trend for κ with increased number of layers. One of the parameters that affects the phonon scattering is crystal anharmonicity which can be evaluated by Umklapp scattering rate. According to Slack’s theory, low anharmonicity leads to a higher thermal conductivity [50]. In monolayer MoSe₂, the phonon scattering is mostly affected by boundary scattering and not by Umklapp scattering, while the effect of Umklapp scattering becomes more significant in few-layered samples that leads to lower thermal conductivity. In addition, due to the effect of imperfections such as point (vacancies, anti-sites, surface contaminants, etc.) and extended defects (grain boundaries, dislocations, edges, etc.) that are not considered completely in theoretical calculations, the measured κ based on experimental measurements is generally lower than the theoretical results [48]. For thicker samples, κ increases with increased thickness. This trend is attributed to the variation of significant surface scattering of long mean free path phonons. For thicker samples, this

surface scattering effect becomes less predominant, so the thermal conductivity is higher. The effect of surface scattering for thicker samples can be illustrated by analyzing the phonon Boltzmann equation using the Landauer approach. Using this approach, the thermal conductivity of the thin film could be written as [25,51–53]:

$$\kappa = K_0 \int M_{\text{ph}}(\varepsilon) \lambda_{\text{ph}}(\varepsilon, T) W_{\text{ph}}(\varepsilon, T) d\varepsilon \quad (7)$$

where $K_0 = \pi^2 k_B^2 T / 3h$ is the quantum of thermal conductance with T being the lattice temperature and W_{ph} is a “window function” given by: $W_{\text{ph}}(\varepsilon, T) = (3\varepsilon / \pi^2 k_B^2 T) [\partial n_{\text{BE}}(\varepsilon, T) / \partial T]$. Also, M_{ph} is the number of conducting modes per cross-sectional area and λ_{ph} is phonon mean free path for both Umklapp phonon-phonon scattering and surface scattering. Here, ε and n_{BE} are the phonon energy and the Bose-Einstein distribution, respectively. Since in this work experiments are conducted at room temperature, laser heating effect is moderate, and phonon dispersion is almost similar for samples with different thickness, the effects of $W_{\text{ph}}(\varepsilon, T)$ and $M_{\text{ph}}(\varepsilon, T)$ are negligible [32]. Therefore, λ_{ph} is the only parameter that needs to be considered. Theoretically, λ_{ph} can be determined using the

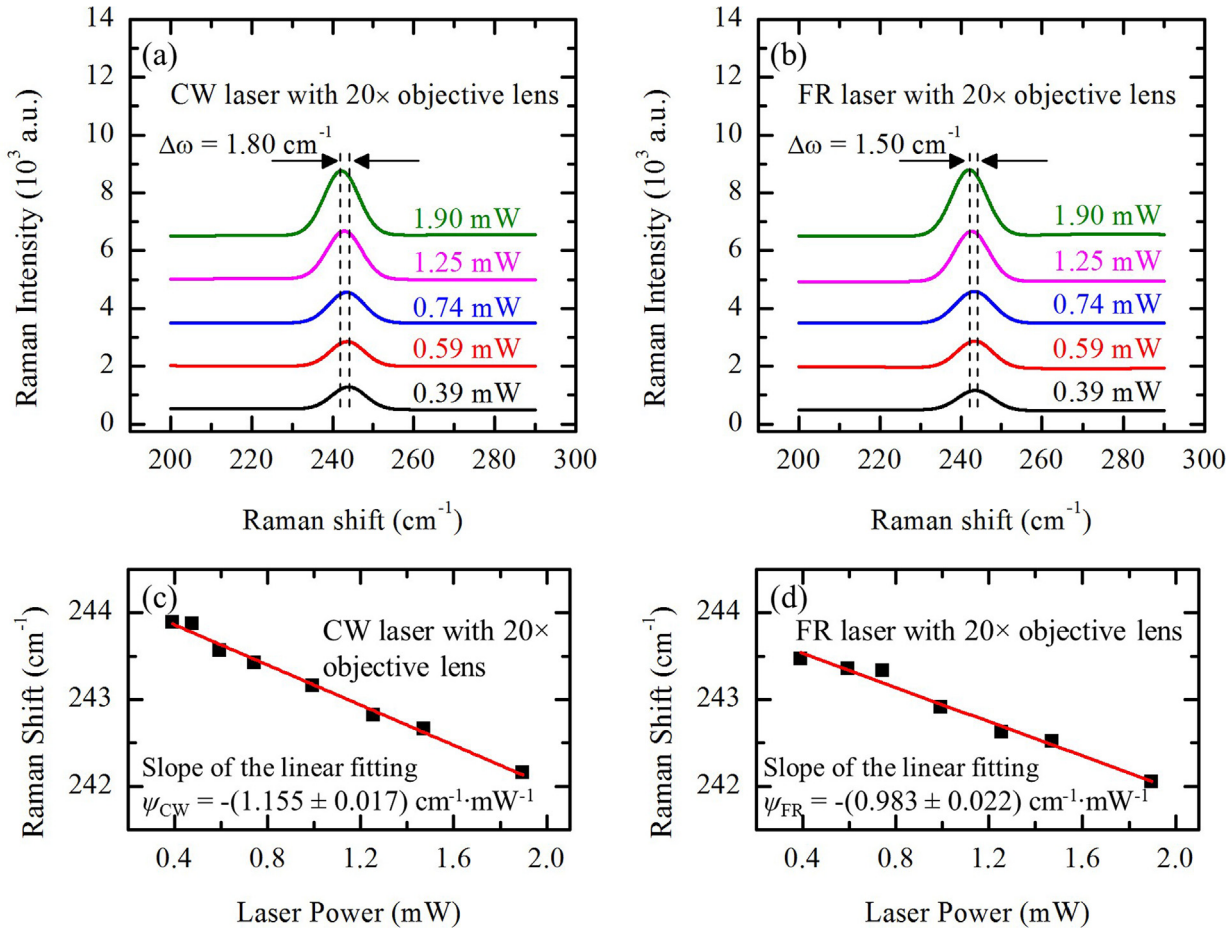


Fig. 5. Raman spectra of 36 nm-thick sample. (a) Five representative Raman spectra of MoSe₂ at increased excitation laser power under 20× laser objective lens with CW laser at room temperature. The total variation of Raman shift for this case is 1.80 cm⁻¹. (b) Five representative Raman spectra of MoSe₂ at increased excitation laser power under 20× laser objective lens with frequency-modulated laser at room temperature. The total variation of Raman shift for this case is 1.50 cm⁻¹. (c) and (d) The Raman shift for A_{1g} mode of MoSe₂ as a function of laser power under 20× objective lens with CW laser and frequency-modulated laser, respectively. Their corresponding linear fitting to obtain the linear power coefficient is also shown in the figures.

Table 2

Summary of the A_{1g} mode RSC values for both CW and FR cases.

Sample thickness (nm)	ψ_{CW} (cm ⁻¹ /mW)	ψ_{FR} (cm ⁻¹ /mW)	Θ
5	-3.558 ± 0.087	-2.694 ± 0.067	0.757 ± 0.026
36	-1.155 ± 0.017	-0.983 ± 0.022	0.851 ± 0.023
55	-0.812 ± 0.019	-0.729 ± 0.016	0.898 ± 0.029
80	-0.645 ± 0.019	-0.602 ± 0.012	0.933 ± 0.033

Fuchs-Sondheimer approach which includes the effect of surface scattering [51,54,55]:

$$\lambda_{ph}(E) = \lambda_{bulk} \left[1 - \frac{3(1-p)}{2\delta} \int_1^\infty \left(\frac{1}{x^3} - \frac{1}{x^5} \right) \frac{1 - e^{-\delta x}}{1 - p e^{-\delta x}} dx \right] \quad (8)$$

where $\delta \equiv (4/3)(t/\lambda_{bulk})$, t is sample thickness, λ_{bulk} is the bulk MFP, and p is the specular parameter in the range 0–1 for completely diffuse to completely specular boundary scattering, respectively. Eq. (8) indicates that for thicker samples, MFP is longer. This means surface scattering is less effective for thicker samples. Conclusively, the in-plane thermal conductivity of thicker samples is higher than the thinner ones. The above two mechanisms combine together to give the nonmonotonic distribution of the thermal conductivity versus thickness: with increased thickness from monolayer to bilayer, the thermal conductivity decreases and reaches a local minimum. After that, with the increased thickness, the thermal conductivity increases. This effect of surface scattering on thermal conductivity

is also observed for few-layered supported and suspended MoSe₂ and MoSe₂ [31,32,56], black phosphorous [25], and few-quintuple-layered Bi₂Te₃ [51]. As shown in Fig. 7(b), the error bar of measured in-plane thermal conductivity becomes larger with increased sample thickness. For thicker samples, since the in-plane thermal conductivity is higher than that of thinner ones, their transient time to reach the steady-state is shorter. As a result, the simulation plot, like Fig. 7(a), becomes flatter when in-plane κ and temperature rise ratio are higher. Therefore, a same amount of uncertainties in RSC value causes larger uncertainties for thicker samples. This effect can be mediated by implementing a higher modulation frequency, like 200 kHz. By doing so, sample has less time to reach the steady-state during each laser on-time period and the ψ_{FR} value will be lower. This will result in a lower error bar for measured κ . Fig. 7(c) shows the thickness dependence of A_{1g} Raman mode of MoSe₂ samples. The samples are excited with 0.46 mW CW laser under 20× objective lens and integrated for 10 s. The blue Raman shift of this peak indicates the increase of interlayer Van der Waals force in MoSe₂ with increased sample layer number [19]. As shown in Fig. 7(c), with the increased thickness from 5 nm to 36 nm, the Raman intensity decreases and then roughly increases for the 55 nm-thick one. This effect is ascribed to several interferences of laser excitation and emitted Raman signal [57–59]. These interferences could be constructive and result in increased the intensity, or destructive that causes decreased the Raman intensity.

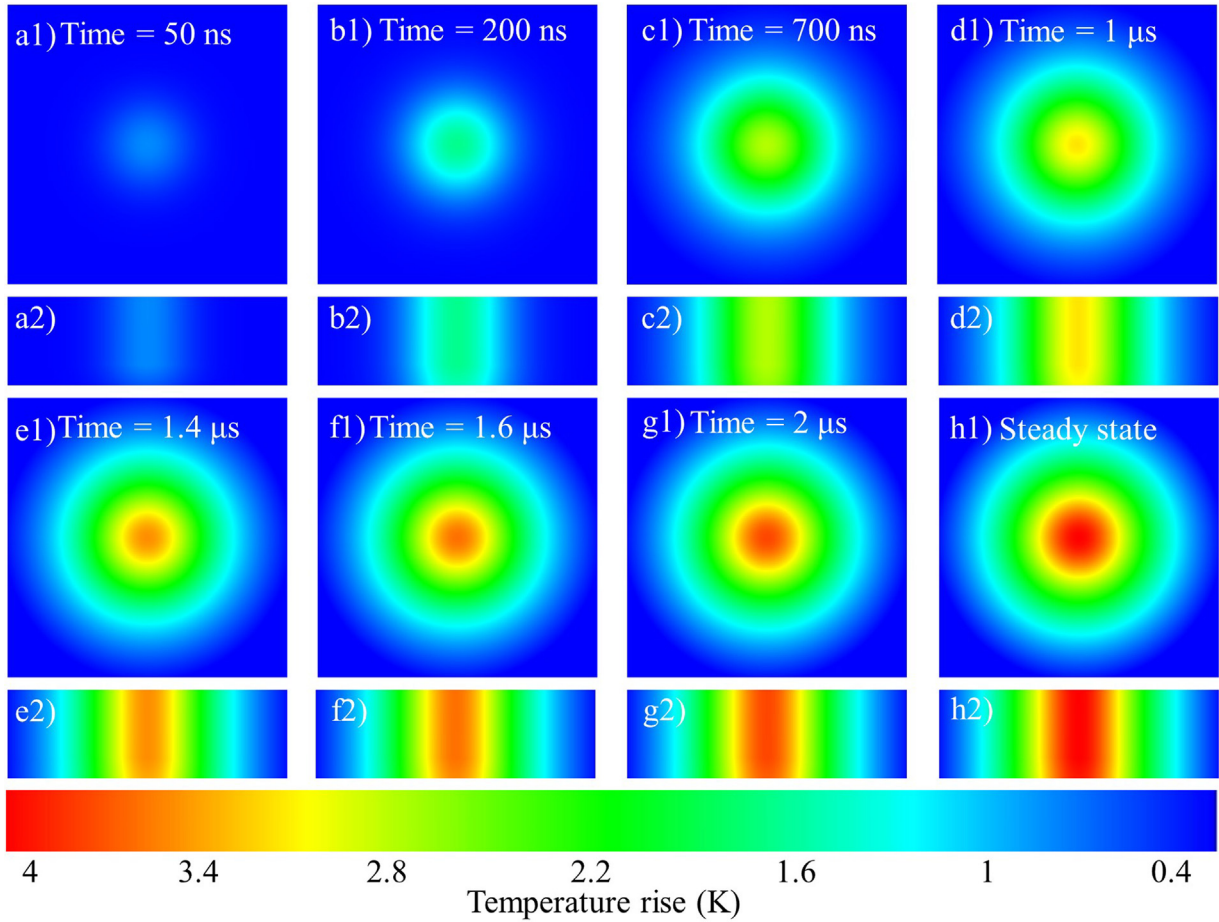


Fig. 6. Temperature rise of the 36 nm sample under laser irradiation as a function of time. The total heating time in each cycle is 5 μ s. Figs. a1–h1 show the temperature rise of the sample top (size: 10 μ m \times 10 μ m). Figs. a2–h2 show the temperature rise of the sample side (cut through the middle of the sample) [size: (horizontal: 10 μ m), (vertical: 36 nm)].

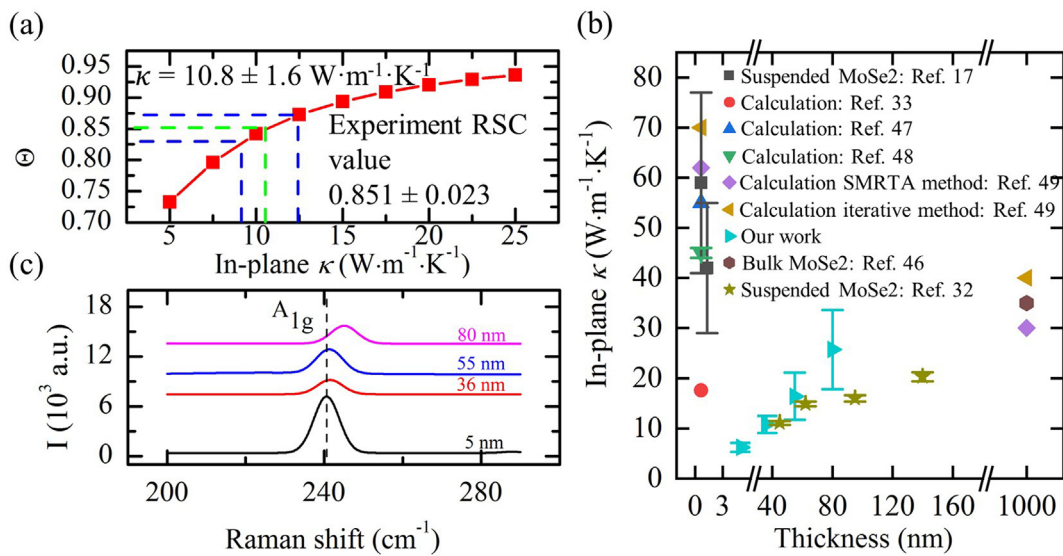


Fig. 7. (a) Results of 3D numerical simulation for the 36 nm-thick MoSe₂ sample. The solid curve demonstrates the theoretical value of temperature rise ratio of FR case to CW case against the in-plane thermal conductivity. Using this curve and the experimental value of temperature rise ratio, the in-plane κ could be interpolated, as indicated with green dashed line. Two blue dashed line demonstrate the uncertainties for in-plane value. (b) Summary of the in-plane κ for the MoSe₂ films in this work and previous studies. (c) The blue shift of Raman peaks with increased sample thickness. (For interpretation of the references to colour in this figure legend, the reader is referred to the web version of this article.)

Table 3
In-plane κ values for all four samples.

Sample thickness (nm)	κ ($\text{W}\cdot\text{m}^{-1}\cdot\text{K}^{-1}$)
5	6.2 ± 0.9
36	10.8 ± 1.7
55	16.4 ± 4.7
80	25.7 ± 7.7

3.3. Discussion of measurement sensitivity: Optical properties, modulation frequency, and sample thickness

In our work, the ρc_p and κ are taken constant in modeling. Here the 36 nm-thick sample is used for assessing this assumption. The Raman shift change ($\Delta\omega$) of this sample under laser irradiation is 1.80 cm^{-1} in CW case. Using this value and Raman temperature coefficient (α) from the references, which is around $0.015 \text{ cm}^{-1}\cdot\text{K}^{-1}$ [17,60,61], we can calculate the temperature rise of the sample under laser spot as $\bar{T}_{Ra} = \Delta\omega/\alpha = 120 \text{ K}$. The average temperature rise of the entire sample determines the level of the thermophysical properties' change. This average temperature is calculated as below

$$\bar{T}_s = \int_0^{r_0} T(r) r dr / \int_0^{r_0} r dr, \quad (9)$$

where r_0 is the radius of the sample. Using these two values and \bar{T}_{CW} that is calculated by Eq. (5), average temperature rise of the sample in all domain under laser irradiation is given by $\bar{T}_{sa} = \bar{T}_s \times (\bar{T}_{Ra}/\bar{T}_{CW})$. Using this equation, \bar{T}_{sa} is calculated as 46.7 K. \bar{T}_{sa} is small enough to make constant κ assumption for all domains. Also, as shown in Fig. 5(c) and (d), the Raman shift change of the FR case is less than the CW's one. Therefore, the average temperature rise of the sample in all domains for FR case (\bar{T}_{fa}) is even less than \bar{T}_{sa} . Kiwia et al. [62] measured the ρc_p of MoSe_2 at different temperatures. While temperature changes by less than 46.7 K, ρc_p changes by less than 2%. It is physically reasonable to assume ρc_p constant during the thermal characterization.

The temperature rise of the sample under laser irradiation depends on both laser propagating downward into the sample

and the laser reflected from the bottom. Fig. 8(a) shows this phenomenon. As shown in Fig. 6, the temperature distribution in the thickness direction is uniform despite the volumetric absorption and the fact that the laser is coming downward. Therefore, it does not matter which direction the laser goes through the sample, the temperature rise is always uniform in the thickness direction, and it is proportional to the laser power. As a consequence, in the FET-Raman technique, the amount of laser reflected does not affect the results and it cancels out during the ratio calculation as below

$$\frac{\Delta T_{tras,FR}}{\Delta T_{tras,CW}} = \frac{\Delta T_{ref,FR}}{\Delta T_{ref,CW}} = \frac{\Delta T_{tras,FR} + \Delta T_{ref,FR}}{\Delta T_{tras,CW} + \Delta T_{ref,CW}}, \quad (10)$$

where $\Delta T_{tras,CW}$ and $\Delta T_{tras,FR}$ are the temperature rise of sample induced by the laser coming downward under both CW and frequency modulated cases, respectively. $\Delta T_{ref,CW}$ and $\Delta T_{ref,FR}$ are the temperature rise of sample induced by the laser coming upward under CW and frequency modulated cases, respectively.

In our FET-Raman, although we use volumetric absorption, the optical absorption depth in fact has very little effect on the determined κ . To demonstrate this, the temperature rise of a sample (36 nm thickness) for different laser absorption depth τ_L and κ values are calculated. Fig. 8(b) shows the temperature rise under CW and FR laser heating, respectively. Both Figures indicate that lower τ_L values cause higher temperature rise because of the higher absorption. Fig. 8(c) shows the theoretical value of temperature rise ratio of FR case to CW case against the in-plane thermal conductivity (left vertical axis) while $\tau_L = 20.6 \text{ nm}$, and percentage change in Θ for several κ and τ_L values (right vertical axis). Θ_0 is regarding the case that $\tau_L = 20.6 \text{ nm}$. This plot shows that effect of τ_L on our calculation is less than 0.4% when the absorption depth is changed from 10 nm to 60 nm. As a result, absorption depth variation changes the thermal conductivity very little and this effect can be neglected. As for the refractive index n , it affects the laser transmitted to the sample and the laser reflected from the bottom. This effect affects both the CW and FR cases with the same ratio, and it will not change Θ nor the final determined κ .

In this work a modulation frequency of 100 kHz is used for all the samples, and we observed a higher uncertainty when the measured thermal conductivity is larger. To explore the effect of modulation frequency on the measurement uncertainty, the

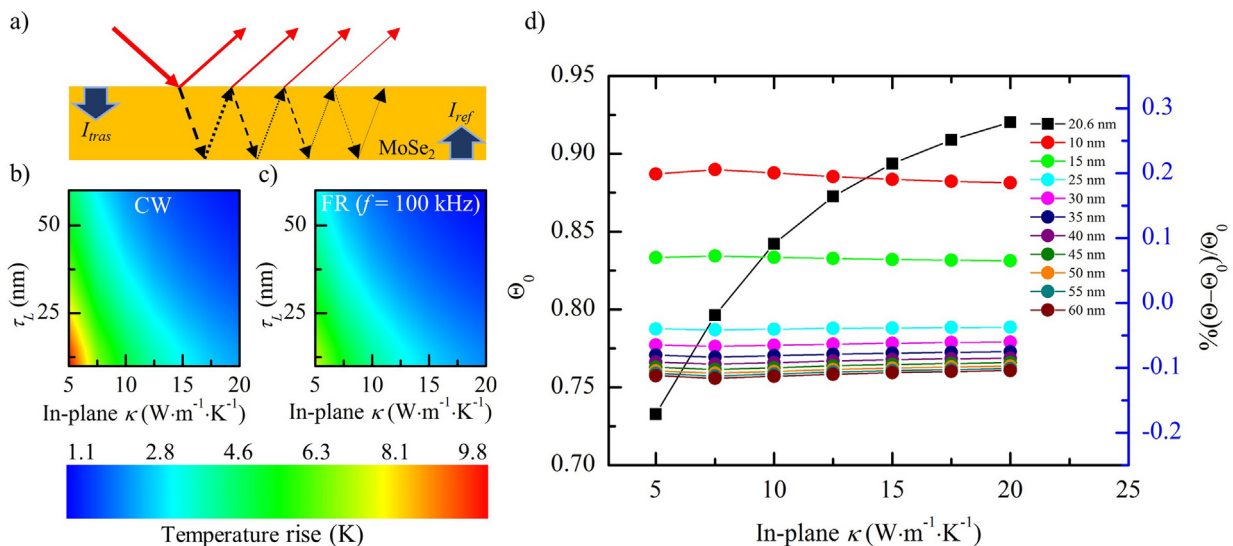


Fig. 8. (a) The transmitted power of at the top surface (I_{tras}), and the reflected power at bottom surface (I_{ref}) of MoSe_2 . Dashed lines represent the laser power propagating downward and dotted lines represent the reflected laser power. (b) and (c) Temperature rise of the 36 nm sample as a function of both laser absorption depth (τ_L) and in-plane thermal conductivity (κ) under both CW and FR laser, respectively. Temperature rise reaches the maximum value when both τ_L and κ are minimum. (d) Variation of Θ with κ (right vertical axis) while $\tau_L = 20.6 \text{ nm}$ and percentage error in Θ when τ_L changes from 10 nm (very low) to 60 nm (very high) (left vertical axis).

uncertainty of measured κ for the 36 nm sample versus different frequencies is calculated, as shown in Fig. 9. Fig. 9(a) shows the theoretical curve Θ versus κ for several frequencies and how the uncertainty of in-plane thermal conductivity is calculated. Here, the uncertainty of Θ for all different frequencies is considered to be 2.7% which is the percentage uncertainty of Θ for the 36 nm sample (Table 2). Also, all the uncertainties are calculated for $\kappa = 10.8 \text{ W}\cdot\text{m}^{-1}\cdot\text{K}^{-1}$ (Table 3). Fig. 9(b) shows the uncertainty of determined κ versus various frequencies. For very low f , as mentioned earlier (in Section 2), sample reaches the steady state temperature. Also, for very high f , since the heating and cooling time is very short, and temperature evolution is very small, so the temperature can be regarded as constant. Therefore, for both high and low

frequencies, temperature remains constant and as a result, theoretical curve of Θ versus κ looks very flat and this causes higher uncertainties. As shown in Fig. 9(b), at $f=190 \text{ kHz}$, the uncertainty reaches a minimum. In this case, the sample has enough time to experience the complete temperature evolution during the transient state and it is not too long to make this transient time negligible in comparison to the whole heating (or cooling) time. Under this optimum frequency, the ratio Θ is 0.75. Therefore, for future FET-Raman studies, it is recommended to adjust the modulation frequency so Θ falls between 0.7 and 0.8 to have a small measurement uncertainty.

The optimized frequency is determined by the combination of thermal conductivity, specific heat, density, and sample lateral

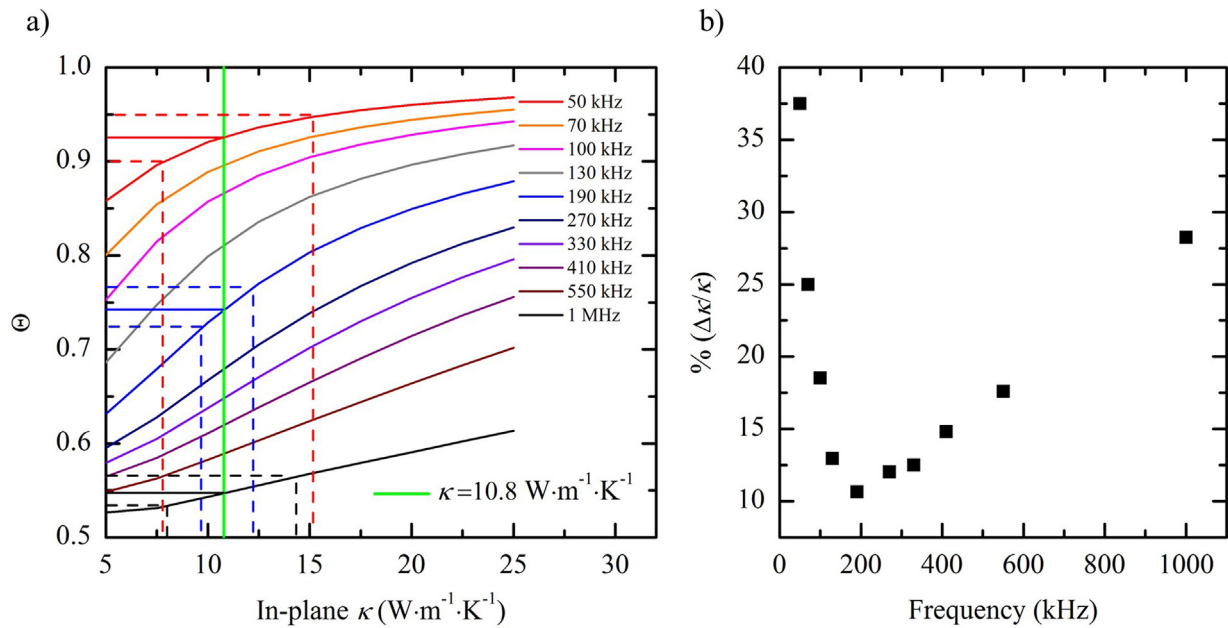


Fig. 9. (a) Theoretical value of normalized RSC (Θ) against the in-plane thermal conductivity under different modulation frequency cases. Also, it indicates how the uncertainty of resulting κ for a constant percent uncertainty of Θ is determined. (b) Percent uncertainty of calculated κ against modulation frequency. For very high or very low f values, $\Delta\kappa/\kappa$ becomes larger, while for the f close to 200 kHz, it reaches a minimum value. This trend can be justified using the fact that for very high or very low f , sample experiences steady state or quasi-steady state that results in an almost constant temperature. The thermal diffusivity has negligible effect under such scenarios.

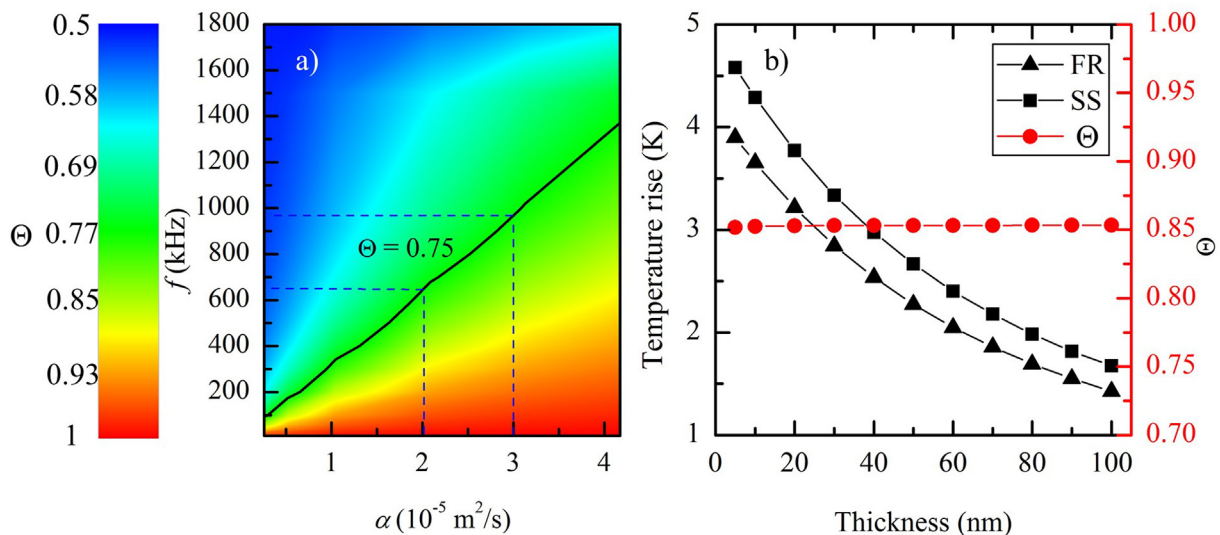


Fig. 10. (a) 3D numerical modeling results for the sample with a thickness 36 nm and $D = 10 \mu\text{m}$. Normalized RSC (Θ) is calculated for different modulation frequencies (f) and thermal diffusivities (α). It shows that for materials with a higher α , the optimized frequency takes larger values. (b) Temperature rise (left vertical axis) and normalized RSC (Θ) (right vertical axis) of several arbitrary samples with thicknesses in range 5–100 nm. In this calculation, $\kappa = 10.8 \text{ W}\cdot\text{m}^{-1}\cdot\text{K}^{-1}$ and $f = 100 \text{ kHz}$.

size. More specifically, the thermal diffusivity directly determines the optimized modulation frequency. To further illustrate the capability of FET-Raman for measuring the thermal conductivity of different materials with various thermal properties, especially thermal diffusivity, we calculated the optimized frequency for several arbitrary materials of different thermal diffusivity. The contour in Fig. 10(a) shows the normalized temperature rise (Θ) as a function of both modulation frequency and α for the 36 nm sample. Also, as mentioned above and illustrated in our previous works, when Θ is in the range of 0.7–0.8, it is most sensitive to f . The solid line indicates the $\Theta = 0.75$. Dashed lines represent the optimized f for two arbitrary materials when α changes from 2×10^{-5} (m^2/s) to 3×10^{-5} (m^2/s). Therefore, for materials with a higher α , like graphene, the optimized f would be higher than materials with lower α .

To investigate the effect of sample thickness on uncertainty of normalized RSC (Θ), the temperature rise under both CW and FR cases and RSC values (Θ) against several arbitrary thicknesses are calculated, as shown in Fig. 10(b). In these calculations, in-plane k and f are set as $10.8 \text{ W}\cdot\text{m}^{-1}\cdot\text{K}^{-1}$ and 100 kHz. The left vertical axis in this figure indicates the temperature rise of the sample under both CW (steady state) and FR cases and it is obvious that by increasing the thickness, they both experience decreasing trends. However, the normalized RSC (Θ) for each thickness (right vertical axis) does not change with thickness. This concludes that the thickness does not affect the measurement of thermal diffusivity in our technique.

4. Conclusion

In this work, a frequency-resolved energy transport technique was successfully developed for characterizing the in-plane thermal conductivity (κ) of nm-thick suspended MoSe_2 samples with different thicknesses. By using this technique, thermal characterization was done by using only one continuous laser source instead of two laser sources. Samples were irradiated under steady-state case using a CW laser and frequency-modulated case using a square-wave modulator. A physical model was developed to simulate both CW and FR cases. Based on the experimental and simulation results, the in-plane thermal conductivity of four MoSe_2 samples were measured using the ratio of two Raman shift power coefficients without knowing the temperature coefficient and laser absorption. κ of MoSe_2 was observed to increase from 6.2 ± 0.9 to $25.7 \pm 7.7 \text{ W}\cdot\text{m}^{-1}\cdot\text{K}^{-1}$ when the sample thickness changes from 5 to 80 nm. Thickness dependency of κ values was explained by the effect of surface phonon scattering which is more dominant for thinner samples. In addition, the larger uncertainties of measured κ for thicker samples were interpreted by effect of modulation frequency on the transient time of temperature evolution. Our sensitivity study showed that the determined κ can be regarded independent of the optical properties. Also, for each sample, there is an optimum modulation frequency under which the measurement has the smallest uncertainty. It is recommended that in FET-Raman characterization, the modulation frequency should be selected to make Θ fall within the range of 0.7–0.8.

Conflict of interest

All authors have no competing interests to declare.

Acknowledgement

Support of this work by Department of Energy (DENE0000671) is gratefully acknowledged.

References

- [1] H. Zhang, M. Chhowalla, Z. Liu, 2D nanomaterials: graphene and transition metal dichalcogenides, *Chem. Soc. Rev.* 47 (2018) 3015–3017.
- [2] W. Zhao, W. Chen, Y. Yue, S. Wu, In-situ two-step Raman thermometry for thermal characterization of monolayer graphene interface material, *Appl. Therm. Eng.* 113 (2017) 481–489.
- [3] H. Malekpour, P. Ramnani, S. Srinivasan, G. Balasubramanian, D.L. Nika, A. Mulchandani, R.K. Lake, A.A. Balandin, Thermal conductivity of graphene with defects induced by electron beam irradiation, *Nanoscale* 8 (2016) 14608–14616.
- [4] A.K. Vallabhaneni, D. Singh, H. Bao, J. Murthy, X. Ruan, Reliability of Raman measurements of thermal conductivity of single-layer graphene due to selective electron-phonon coupling: a first-principles study, *Phys. Rev. B* 93 (2016) 125432.
- [5] A.A. Balandin, S. Ghosh, W. Bao, I. Calizo, D. Teweldebrhan, F. Miao, C.N. Lau, Superior thermal conductivity of single-layer graphene, *Nano Lett.* 8 (2008) 902–907.
- [6] D.L. Nika, A.A. Balandin, Phonons and thermal transport in graphene and graphene-based materials, *Rep. Prog. Phys.* 80 (2017) 036502.
- [7] B. Smith, B. Vermeersch, J. Carrete, E. Ou, J. Kim, N. Mingo, D. Akinwande, L. Shi, Temperature and thickness dependences of the anisotropic in-plane thermal conductivity of black phosphorus, *Adv. Mater.* 29 (2017).
- [8] X. Liu, C.R. Ryder, S.A. Wells, M.C. Hersam, Resolving the In-Plane Anisotropic Properties of Black Phosphorus, *Small Methods*, 2017.
- [9] H. Jang, J.D. Wood, C.R. Ryder, M.C. Hersam, D.G. Cahill, Anisotropic thermal conductivity of exfoliated black phosphorus, *Adv. Mater.* 27 (2015) 8017–8022.
- [10] B. Sun, X. Gu, Q. Zeng, X. Huang, Y. Yan, Z. Liu, R. Yang, Y.K. Koh, Temperature dependence of anisotropic thermal-conductivity tensor of bulk black phosphorus, *Adv. Mater.* 29 (2017).
- [11] S. Das, H.-Y. Chen, A.V. Penumatcha, J. Appenzeller, High performance multilayer MoS_2 transistors with scandium contacts, *Nano Lett.* 13 (2012) 100–105.
- [12] H. Li, J. Wu, Z. Yin, H. Zhang, Preparation and applications of mechanically exfoliated single-layer and multilayer MoS_2 and WSe_2 nanosheets, *Acc. Chem. Res.* 47 (2014) 1067–1075.
- [13] E. Yalon, C.J. McClellan, K.K. Smithe, M. Muñoz Rojo, R.L. Xu, S.V. Suryavanshi, A.J. Gabourie, C.M. Neumann, F. Xiong, A.B. Farimani, Energy dissipation in monolayer MoS_2 electronics, *Nano Lett.* 17 (2017) 3429–3433.
- [14] M. Yarali, H. Brahmi, Z. Yan, X. Li, L. Xie, S. Chen, S. Kumar, M. Yoon, K. Xiao, A. Mavrokefalos, The effect of metal doping and vacancies on the thermal conductivity of monolayer molybdenum diselenide, *ACS Appl. Mater. Interf.* (2018).
- [15] R. Yan, J.R. Simpson, S. Bertolazzi, J. Brivio, M. Watson, X. Wu, A. Kis, T. Luo, A.R. Hight Walker, H.G. Xing, Thermal conductivity of monolayer molybdenum disulfide obtained from temperature-dependent Raman spectroscopy, *ACS Nano* 8 (2014) 986–993.
- [16] S. Sahoo, A.P. Gaur, M. Ahmadi, M.J.-F. Guinel, R.S. Katiyar, Temperature-dependent Raman studies and thermal conductivity of few-layer MoS_2 , *J. Phys. Chem. C* 117 (2013) 9042–9047.
- [17] X. Zhang, D. Sun, Y. Li, G.-H. Lee, X. Cui, D. Chenet, Y. You, T.F. Heinz, J.C. Hone, Measurement of lateral and interfacial thermal conductivity of single- and bilayer MoS_2 and MoSe_2 using refined optothermal Raman technique, *ACS Appl. Mater. Interf.* 7 (2015) 25923–25929.
- [18] W. Cai, A.L. Moore, Y. Zhu, X. Li, S. Chen, L. Shi, R.S. Ruoff, Thermal transport in suspended and supported monolayer graphene grown by chemical vapor deposition, *Nano Lett.* 10 (2010) 1645–1651.
- [19] P. Yuan, C. Li, S. Xu, J. Liu, X. Wang, Interfacial thermal conductance between few to tens of layered- MoS_2 and c-Si: effect of MoS_2 thickness, *Acta Mater.* 122 (2017) 152–165.
- [20] X. Tang, S. Xu, X. Wang, Corrugated epitaxial graphene/ SiC interfaces: photon excitation and probing, *Nanoscale* 6 (2014) 8822–8830.
- [21] A.A. Balandin, Thermal properties of graphene and nanostructured carbon materials, *Nat. Mater.* 10 (2011) 569.
- [22] H. Malekpour, A.A. Balandin, Raman-based technique for measuring thermal conductivity of graphene and related materials, *J. Raman Spectrosc.* 49 (2018) 106–120.
- [23] J.-U. Lee, D. Yoon, H. Kim, S.W. Lee, H. Cheong, Thermal conductivity of suspended pristine graphene measured by Raman spectroscopy, *Phys. Rev. B* 83 (2011) 081419.
- [24] N. Peimyoo, J. Shang, W. Yang, Y. Wang, C. Cong, T. Yu, Thermal conductivity determination of suspended mono- and bilayer WS_2 by Raman spectroscopy, *Nano Res.* 8 (2015) 1210–1221.
- [25] Z. Luo, J. Maassen, Y. Deng, Y. Du, R.P. Garrelts, M.S. Lundstrom, D.Y. Peide, X. Xu, Anisotropic in-plane thermal conductivity observed in few-layer black phosphorus, *Nat. Commun.* 6 (2015) 8572.
- [26] S. Xu, T. Wang, D. Hurlley, Y. Yue, X. Wang, Development of time-domain differential Raman for transient thermal probing of materials, *Opt. Exp.* 23 (2015) 10040–10056.
- [27] C. Li, S. Xu, Y. Yue, B. Yang, X. Wang, Thermal characterization of carbon nanotube fiber by time-domain differential Raman, *Carbon* 103 (2016) 101–108.
- [28] T. Wang, S. Xu, D.H. Hurlley, Y. Yue, X. Wang, Frequency-resolved Raman for transient thermal probing and thermal diffusivity measurement, *Opt. Lett.* 41 (2016) 80–83.

- [29] T. Wang, M. Han, R. Wang, P. Yuan, S. Xu, X. Wang, Characterization of anisotropic thermal conductivity of suspended nm-thick black phosphorus with frequency-resolved Raman spectroscopy, *J. Appl. Phys.* 123 (2018) 145104.
- [30] P. Yuan, R. Wang, H. Tan, T. Wang, X. Wang, Energy transport state resolved raman for probing interface energy transport and hot carrier diffusion in few-layered MoS₂, *ACS Photon.* 4 (2017) 3115–3129.
- [31] P. Yuan, R. Wang, T. Wang, X. Wang, Y. Xie, Nonmonotonic thickness-dependence of in-plane thermal conductivity of few-layered MoS₂: 2.4 to 37.8 nm, *Phys. Chem. Chem. Phys.* 20 (2018) 25752–25761.
- [32] R. Wang, T. Wang, H. Zobeiri, P. Yuan, C. Deng, Y. Yue, S. Xu, X. Wang, Measurement of thermal conductivity of suspended MoS₂ and MoSe₂ by nanosecond ET-Raman free of temperature calibration and laser absorption evaluation, *Nanoscale* (2018).
- [33] B. Peng, H. Zhang, H. Shao, Y. Xu, X. Zhang, H. Zhu, Thermal conductivity of monolayer MoS₂, MoSe₂, and WS₂: interplay of mass effect, interatomic bonding and anharmonicity, *RSC Adv.* 6 (2016) 5767–5773.
- [34] A. Blinder, A. Bolgar, Z.A. Trofimova, Thermodynamic properties of selenides of transition metals, *Powder Metall. Metal Ceram.* 32 (1993) 234–239.
- [35] P. Yuan, J. Liu, R. Wang, X. Wang, The hot carrier diffusion coefficient of sub-10 nm virgin MoS₂: uncovered by non-contact optical probing, *Nanoscale* 9 (2017) 6808–6820.
- [36] X. Chen, X. Wang, Microscale spatially resolved thermal response of Si nanotip to laser irradiation, *J. Phys. Chem. C* 115 (2011) 22207–22216.
- [37] C. Yim, M. O'Brien, N. McEvoy, S. Winters, I. Mirza, J.G. Lunney, G.S. Duesberg, Investigation of the optical properties of MoS₂ thin films using spectroscopic ellipsometry, *Appl. Phys. Lett.* 104 (2014) 103114.
- [38] H.-L. Liu, C.-C. Shen, S.-H. Su, C.-L. Hsu, M.-Y. Li, L.-J. Li, Optical properties of monolayer transition metal dichalcogenides probed by spectroscopic ellipsometry, *Appl. Phys. Lett.* 105 (2014) 201905.
- [39] S. Sinha, Thermal model for nanosecond laser ablation of alumina, *Ceram. Int.* 41 (2015) 6596–6603.
- [40] P. Tonndorf, R. Schmidt, P. Böttger, X. Zhang, J. Börner, A. Liebig, M. Albrecht, C. Kloc, O. Gordan, D.R. Zahn, Photoluminescence emission and Raman response of monolayer MoS₂, MoSe₂, and WSe₂, *Opt. Exp.* 21 (2013) 4908–4916.
- [41] S. Tongay, J. Zhou, C. Ataca, K. Lo, T.S. Matthews, J. Li, J.C. Grossman, J. Wu, Thermally driven crossover from indirect toward direct bandgap in 2D semiconductors: MoSe₂ versus MoS₂, *Nano Lett.* 12 (2012) 5576–5580.
- [42] R. Long, O.V. Prezhdo, Quantum coherence facilitates efficient charge separation at a MoS₂/MoSe₂ van der Waals junction, *Nano Lett.* 16 (2016) 1996–2003.
- [43] M.J. Shin, D.H. Kim, D. Lim, Photoluminescence saturation and exciton decay dynamics in transition metal dichalcogenide monolayers, *J. Korean Phys. Soc.* 65 (2014) 2077–2081.
- [44] L. Ruan, H. Zhao, D. Li, S. Jin, S. Li, L. Gu, J. Liang, Enhancement of thermoelectric properties of molybdenum diselenide through combined mg intercalation and Nb doping, *J. Electron. Mater.* 45 (2016) 2926–2934.
- [45] Y. Chen, G. Jiang, S. Chen, Z. Guo, X. Yu, C. Zhao, H. Zhang, Q. Bao, S. Wen, D. Tang, D. Fan, Mechanically exfoliated black phosphorus as a new saturable absorber for both Q-switching and Mode-locking laser operation, *Opt. Exp.* 23 (2015) 12823–12833.
- [46] P. Jiang, X. Qian, X. Gu, R. Yang, Probing anisotropic thermal conductivity of transition metal dichalcogenides MX₂ (M= Mo, W and X= S, Se) using time-domain thermoreflectance, *Adv. Mater.* 29 (2017) 1701068.
- [47] X. Gu, R. Yang, Phonon transport in single-layer transition metal dichalcogenides: a first-principles study, *Appl. Phys. Lett.* 105 (2014) 131903.
- [48] A. Kandemir, H. Yapicioglu, A. Kinaci, T. Çağın, C. Sevik, Thermal transport properties of MoS₂ and MoSe₂ monolayers, *Nanotechnology* 27 (2016) 055703.
- [49] S. Kumar, U. Schwingschlogl, Thermoelectric response of bulk and monolayer MoSe₂ and WSe₂, *Chem. Mater.* 27 (2015) 1278–1284.
- [50] G.A. Slack, Nonmetallic crystals with high thermal conductivity, *J. Phys. Chem. Solids* 34 (1973) 321–335.
- [51] M.T. Pettes, J. Maassen, I. Jo, M.S. Lundstrom, L. Shi, Effects of surface band bending and scattering on thermoelectric transport in suspended bismuth telluride nanoplates, *Nano Lett.* 13 (2013) 5316–5322.
- [52] C. Jeong, S. Datta, M. Lundstrom, Thermal conductivity of bulk and thin-film silicon: a Landauer approach, *J. Appl. Phys.* 111 (2012) 093708.
- [53] C. Jeong, S. Datta, M. Lundstrom, Full dispersion versus Debye model evaluation of lattice thermal conductivity with a Landauer approach, *J. Appl. Phys.* 109 (2011) 073718.
- [54] K. Fuchs, The conductivity of thin metallic films according to the electron theory of metals, in: *Mathematical Proceedings of the Cambridge Philosophical Society*, Cambridge University Press, 1938, pp. 100–108.
- [55] E.H. Sondheimer, The mean free path of electrons in metals, *Adv. Phys.* 1 (1952) 1–42.
- [56] J.J. Bae, H.Y. Jeong, G.H. Han, J. Kim, H. Kim, M.S. Kim, B.H. Moon, S.C. Lim, Y.H. Lee, Thickness-dependent in-plane thermal conductivity of suspended MoS₂ grown by chemical vapor deposition, *Nanoscale* 9 (2017) 2541–2547.
- [57] C. Lee, H. Yan, L.E. Brus, T.F. Heinz, J. Hone, S. Ryu, Anomalous lattice vibrations of single- and few-layer MoS₂, *ACS Nano* 4 (2010) 2695–2700.
- [58] X. Tang, S. Xu, J. Zhang, X. Wang, Five orders of magnitude reduction in energy coupling across corrugated graphene/substrate interfaces, *ACS Appl. Mater. Interf.* 6 (2014) 2809–2818.
- [59] Y. Wang, Z. Ni, Z. Shen, H. Wang, Y. Wu, Interference enhancement of Raman signal of graphene, *Appl. Phys. Lett.* 92 (2008) 043121.
- [60] D.J. Late, S.N. Shirodkar, U.V. Waghmare, V.P. Dravid, C. Rao, Thermal expansion, anharmonicity and temperature-dependent raman spectra of single- and few-layer MoSe₂ and WSe₂, *ChemPhysChem* 15 (2014) 1592–1598.
- [61] M. Yang, X. Cheng, Y. Li, Y. Ren, M. Liu, Z. Qi, Anharmonicity of monolayer MoS₂, MoSe₂, and WSe₂: a Raman study under high pressure and elevated temperature, *Appl. Phys. Lett.* 110 (2017) 093108.
- [62] H.L. Kiwia, E.F. Westrum Jr, Low-temperature heat capacities of molybdenum diselenide and ditelluride, 1975.